PNAS RESEARCH ARTICLE | EARTH, ATMOSPHERIC, AND PLANETARY SCIENCES

Micromechanical modeling of triphasic granular media

Amiya Prakash Das[a], Jidong Zhao[a,1], and Thomas Sweijen[b]

Affiliations are included on p. 10.

Edited by David Weitz, Harvard University, Cambridge, MA; received October 3, 2024; accepted April 8, 2025

This paper presents pore unit assembly-discrete element model (PUA-DEM), a pore-scale hydromechanical framework that resolves interactions between mobile granular particles and multiphase fluids in unsaturated granular media. The framework uniquely integrates DEM with pore-scale hydrodynamic models to capture unsaturated flow dynamics, while leveraging a two-way coupling mechanism to ensure bidirectional fluid–grain feedback through stabilized domain partitioning. Further innovations include a dynamic pore-merging and retriangulation algorithm that enhances computational efficiency for large-scale systems. Validated against experimental data for glass beads and Ottawa sand, PUA-DEM accurately reproduces critical hydromechanical phenomena-including capillary/viscous fingering, wetting-induced granular swelling/collapse, and quasi-static deformation-under diverse saturation and loading regimes. Numerical case studies reveal how capillary forces and wetting fluid saturation collectively govern granular response, from pore-scale meniscus evolution to macroscale flow instabilities. By bridging pore- and particle-scale physics, PUA-DEM advances predictive modeling of partially saturated granular systems, offering transformative insights for geohazard mitigation, sustainable agriculture, pharmaceutical manufacturing, and energy-related engineering applications.

granular media | fluid flow | capillarity | hydromechanical coupling | DEM

Significance

Granular materials-from soils to pharmaceutical powders-exhibit mechanical behavior governed by interaction between solid grains and interstitial fluids. Capillary forces critically control these systems, yet their multiscale dependencies on saturation, pore structure, and stress remain unpredictable due to difficulties for resolving bidirectional coupling between multiphase fluids and granular particles. We present pore unit assembly-discrete element model (PUA-DEM), a computational framework integrating DEM with pore-scale hydromechanics. It explicitly resolves air–water interfaces, fluid transport, and grain dynamics, capturing how fluid menisci and particle rearrangements govern deformation and flow. PUA-DEM bridges microscale interactions to emergent macroscopic behavior in unsaturated granular media. This advance unlocks predictive modeling of multiphase granular system and offers critical insights for geohazard mitigation, agricultural sustainability, and pharmaceutical powder processing.

Fluid flow through granular media governs critical processes in soil mechanics (1, 2), hydrogeology (3), carbon sequestration (4, 5), energy extraction (6, 7). These systems commonly exhibit multiscale transport phenomena, ranging from Darcy-scale flow to pore-scale dynamics such as dissolution, suffusion, suffosion, and interfacial reactions (8–11). A fundamental challenge in computational modeling of these systems lies in accurate consideration of the bidirectional coupling between fluid flow and evolving pore structures formed by deformable grain skeletons, particularly in unsaturated multiphase systems where capillary, viscous, and inertial forces compete across spatial and temporal scales (12–14).

Existing numerical approaches face inherent trade-offs between fidelity and computational feasibility. Continuum methods like finite element modeling (FEM) (15) and computational fluid dynamics (CFD) (16, 17) employ constitutive relations to approximate the hydromechanical behavior, yet struggle to resolve localized fluid–solid interactions at pore- and particle-scales or reconcile debated effective stress definitions (18–22). Discrete element methods (DEM) excel at capturing particle-scale mechanics but encounter limitations in representing complex fluid morphologies and flow mechanisms such as trimers and pentamers, particularly at high saturation (23–28). Hybrid approaches coupling DEM with pore-resolving techniques [e.g., Lattice Boltzmann Methods (29–36) or volume of fluid method (37, 38)] help to improve interfacial tracking but remain computationally prohibitive for large-scale systems. Recent advances in pore-network modeling (39–43) balance efficiency and physical detail but often neglect fabric structure and stress anisotropy or rely on one-way coupling assumptions (44–46).

We present the pore unit assembly-discrete element model (PUA-DEM), a fully coupled hydromechanical framework integrating grain-scale mechanics and pore-resolved hydrodynamics for unsaturated granular systems. Building on unsaturated flow models (40, 45, 47–49), PUA-DEM unifies DEM for granular dynamics with a dynamic pore-network solver to resolve multiphase fluid interactions. The void space is discretized via regular triangulation (RT) into tetrahedral pore units, enabling precise geometric representations of pore structures and fluid pathways. A pore-merging algorithm consolidates overlapping tetrahedra, while dynamic retriangulation adapts to large deformations. Two-phase flows are resolved via an implicit pressure explicit saturation (IMPES) scheme, accounting for capillary pressure, saturation-dependent hydraulic

The authors declare no competing interest.

This article is a PNAS Direct Submission.

[1]To whom correspondence may be addressed. Email: jzhao@ust.hk.

This article contains supporting information online at https://www.pnas.org/lookup/suppl/doi:10.1073/pnas.2420314122/-/DCSupplemental.

Published May 2, 2025.

conductivity, and deformation-coupled hydromechanics. Bidirectional hydromechanical coupling is achieved by projecting fluid forces onto DEM particles, updating positions and pore geometries iteratively. Fig. 1 shows a schematic overview of the framework. Full implementation details are provided in *Materials and Methods* and *SI Appendix*.

This approach introduces three critical quantifiable advancements: 1) explicit resolution of capillary force anisotropy gover ning triphasic stress distributions, 2) dynamic two-way coupling between fluid redistribution and fabric evolution, and 3) saturation-regime adaptability. These advancements empower PUA-DEM to simulate intricate fluid–solid interactions with high fidelity across diverse scenarios. The following five case studies demonstrate its predictive capabilities in addressing challenges inadequately resolved by existing methods while providing novel grain- and pore-scale insights into unsaturated granular media: a) drainage and imbibition cycles, b) capillary versus viscous fingering dynamics, c) confined granular swelling in unsaturated flow, d) 1D desaturation under controlled drainage, and e) wetting-induced structural collapse. One-way coupling is considered for Cases (a) and (b), and two-way coupling for (c) to (e).

Drainage and Imbibition Dynamics

Simulations. The coupled PUA-DEM framework was first validated against the drainage and imbibition experiments by Culligan et al. (50), focusing on elucidating the link between macroscopic observations with pore-scale drainage and imbibition dynamics. The experiments investigated fluid displacement in a cylindrical glass bead column (70 mm height, 7 mm diameter). To replicate these conditions computationally, we adopted the same grain size distribution reported in the experiments (30 wt% particles: 1.0 to 1.4 mm, 35 wt%: 0.85 mm, 35 wt%: 0.60 mm) but employed a cubic specimen with the identical initial porosity (0.34) for computational efficiency. The initial polydisperse DEM packing was generated using the dynamic compaction protocol from ref. 51, progressively adjusting the interparticle friction and the confining pressure to achieve a homogeneous, statistically representative assembly. The final packing, under 10 kPa confining pressure and fixed with an interparticle fiction angle of 30°. For the drainage scenario, water was incrementally withdrawn from a fully saturated packing to simulate air invasion (drainage), capturing the transition from saturated to unsaturated states.

Fig. 3*A* illustrates the simulated DEM packing. The top boundary is connected to a nonwetting reservoir (referred to as air) at pressure p^{air}, while the bottom boundary is linked to a wetting reservoir (referred to as water) maintained at a constant pressure p^{w}. All other boundaries are impermeable. The specimen is initially fully saturated, except for the top row of pores connected to the air reservoir, which are initialized with a small air fraction of 1.0×10^{-6}. Drainage is induced by gradually decreasing the water pressure, while the air pressure is held constant at 0 Pa. To expedite equilibrium convergence before each pressure increment, a global pressure difference, p^{c}_{global}, is applied. This process is repeated to increase p^{c}_{global} from 400 to 1,300 Pa in 100 Pa steps until the capillary pressure–saturation curve is fully reproduced. For validation purposes, all particles in the specimen were immobilized during drainage, resulting in a one-way coupling scenario. Primary drainage, represented by the red dashed line in Fig. 2*A*, begins when water is progressively displaced with increased capillary pressure. Imbibition occurs as capillary pressure decreases, allowing water to reoccupy pore spaces while air becomes trapped due to snap-off (52, 53). Secondary drainage begins after imbibition and exhibits a distinct retention behavior, as indicated by the black dashed line in Fig. 2*A*. These curves replicate the capillary pressure–saturation relationships across different saturation cycles, capturing the influence of pore-scale fluid distributions on retention characteristics.

Macroscopic predictions. Fig. 2*A* compares the simulation results for the drainage, imbibition, and secondary drainage stages with the experimental $(p^{c} - S_{r})$ data reported by Culligan et al. (50).

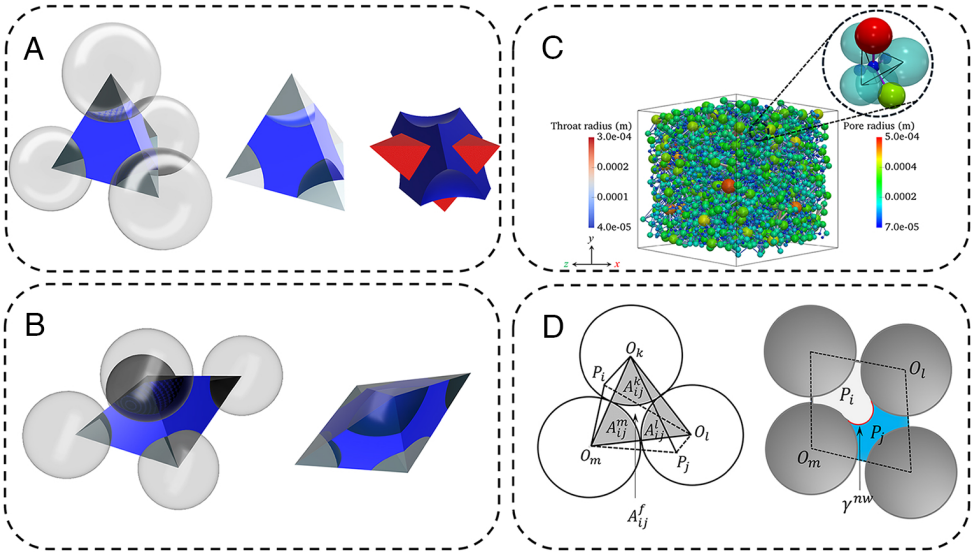

Fig. 1. Illustration of the PUA-DEM Approach: (*A*) The pore units generated by the RT method, depicted in blue with their irregular geometries, are replaced by a pore unit with a regular polygonal shape, shown in red. (*B*) The pore merging process, where two overlapping pore units are combined into a higher-dimensional pore unit. (*C*) A stick-ball representation of the pore network, where spheres represent pores connected to neighboring pore units by tube elements, with each tube's radius corresponding to the pore throat. The callout highlights a grain-based tetrahedron featuring DEM particles at its vertices (indicated in cyan), which are interconnected to neighboring pore units through the tube elements. (*D*) The fluid force model, illustrating the forces exerted by the pressure (*p*) on a particle (*k*) and the interfacial tension forces at the fluid-solid boundary.

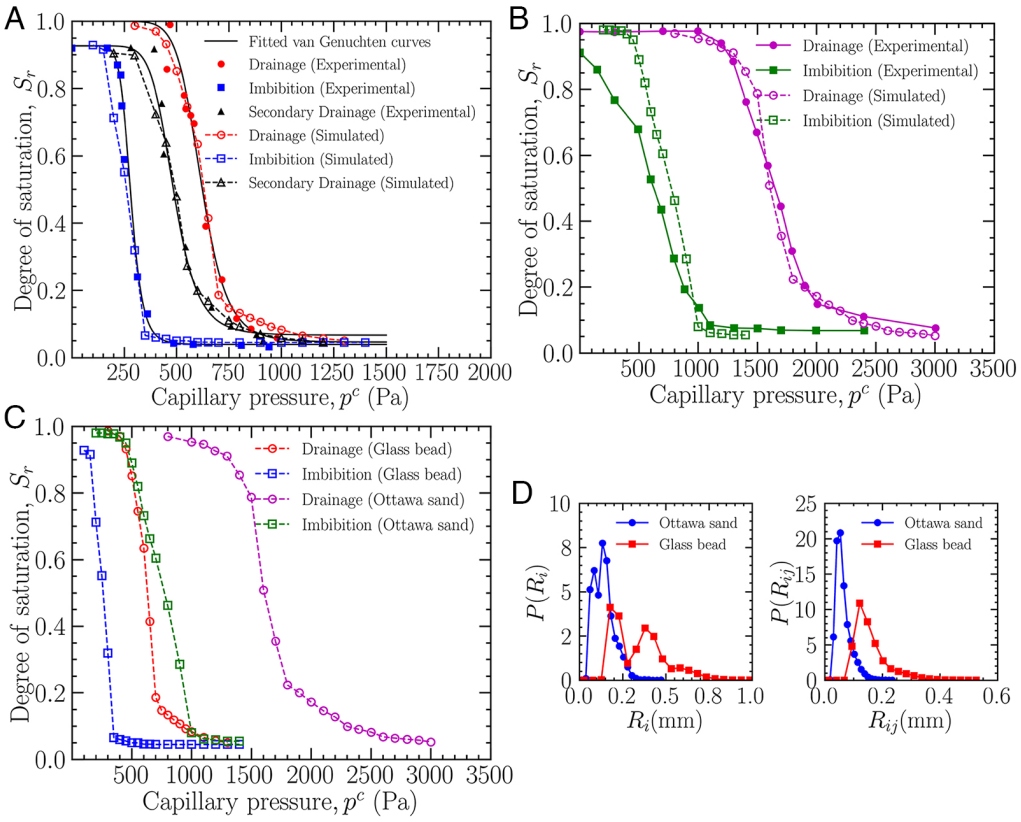

Fig. 2. (*A*) Comparison of simulated capillary pressure curves for fluid–fluid displacement processes (drainage, imbibition, and secondary drainage) against experimental data from ref. 50, with van Genuchten model fits for the soil–water characteristic curve (SWCC). (*B*) Simulated drainage and imbibition curves for Ottawa sand show close agreement with experimental results from ref. 54. (*C*) Simulated water retention curves for glass beads (50) and Ottawa sand (54), highlighting material-specific differences in capillary behavior. (*D*) Distributions of pore radius R_i (*Left*) and throat size R_{ij} (*Right*) for glass beads and Ottawa sand.

The experimental capillary pressure–saturation relationship was fitted using the van Genuchten model (2):

$$S_r = \frac{1}{\left(1 + |\alpha p^c|^n\right)^m}, \quad [1]$$

where α (units: Pa^{-1}) represents the inverse of the entry pressure, while n and m are empirical parameters governing the pore size distribution. The strong agreement between numerical predictions and experimental data validates the accuracy of the proposed PUA-DEM.

The framework was further employed to predict the $(p^c - S_r)$ relations for Ottawa sand using a spherical packing with porosity identical to that reported in the X-ray computed tomography experiments by Mohsin et al. (54). Fig. 2*B* presents a comparison of the numerical and experimental results. While the numerically predicted drainage curve aligns well with the experimental data, the imbibition curve matches the experimental trend only up to a saturation degree of 0.4. Beyond this point, the numerical model overpredicts saturation compared to the experimental results. This discrepancy may stem from numerical approximation of the irregular geometry of real sand particles with idealized spheres. Fig. 2*C* provides a comparative analysis of predictions for glass beads and Ottawa sand. Notably, Ottawa sand exhibits higher fluid retention than glass beads during drainage and imbibition, leading to a broader hysteresis loop. This distinction arises from the contrasting pore structures of the two materials, as illustrated in Fig. 2*D*. During drainage, fluid retention is governed primarily by the distribution of pore throats, whereas imbibition is influenced by the distribution of pore radii. Ottawa sand, characterized by a narrower range of smaller pore bodies and tighter sizes, requires higher capillary pressures for fluid displacement due to increased resistance to flow through these constricted pore spaces. The observed $p^c - S_r$ hysteresis reflects conventional behavior in dynamic porous media. In inert systems (i.e., systems where the configuration of the solid skeleton or the wetting properties remain unchanged), recent work demonstrates an absence of such capillary pressure hysteresis (55). This discrepancy may be addressed by using more geometric-related state descriptions, such as the Minkowski functionals.

Pore-scale fluid dynamics. The drainage and imbibition processes illustrated above highlight intriguing pore-scale physics. As depicted in Fig. 3*A*, during the initiation of drainage, water is gradually displaced from the top boundary by air connected to the top inlet reservoir. This process is driven by a negligibly low flow rate and increasing capillary pressure to ensure viscous forces remain insignificant (8, 45, 48). Drainage continues as air displaces water from adjacent pores or throats with the largest radii once the capillary pressure exceeds the threshold that a pore–throat interface can sustain (Fig. 3 *B* and *C*). Note that during primary drainage, air invades throats and pores accessible under the prevailing capillary pressure; however, during secondary drainage, air may already reside as trapped residual fluid that has undergone snap-off by water invasion from prior imbibition.

When pore bodies exceed throat sizes, air can abruptly invade neighboring pores via Haines jump (56, 57), driven by instabilities in capillary equilibrium. Notably, capillary pressure may temporarily decrease if air enters a larger pore after traversing

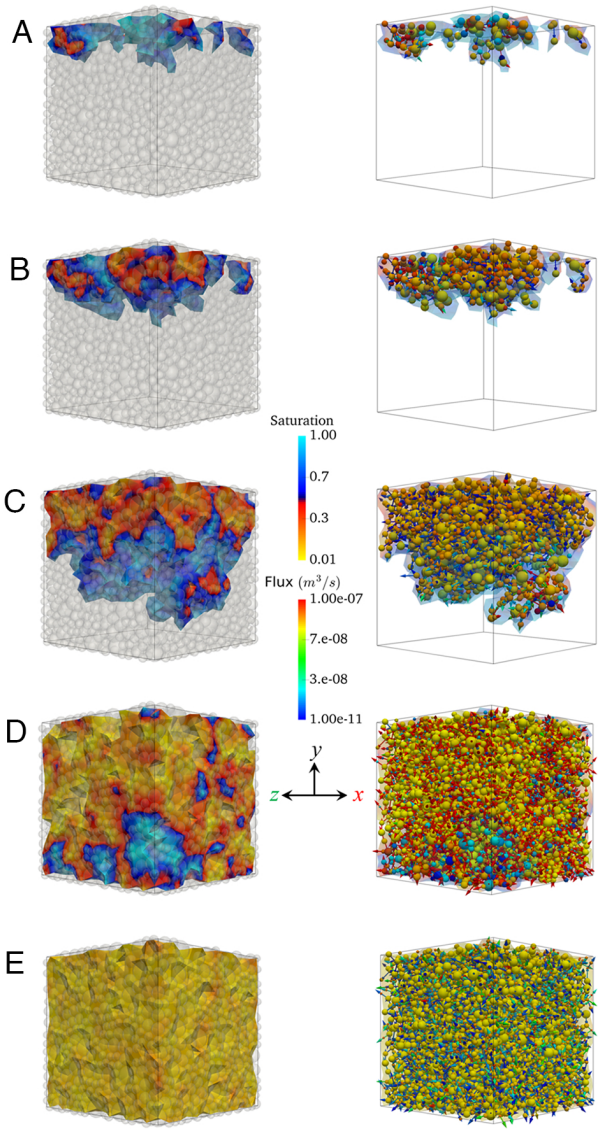

Fig. 3. Visualization of drainage dynamics in glass beads. *Left* panels: Fluid configuration color-coded by wetting fluid saturation. *Right* panels: Fluid flux vectors indicating invasion pathways, with color intensity scaling with flux magnitude. Pores are represented as spheres, color-mapped to local wetting fluid saturation at progressive drainage stages: (*A*) $S_r = 0.97$, (*B*) $S_r = 0.80$, (*C*) $S_r = 0.62$, (*D*) $S_r = 0.24$, and (*E*) $S_r = 0.065$.

a narrower throat, potentially causing retraction from previously invaded regions to reestablish equilibrium (48, 58, 59). Throughout invasion percolation, the air–water interface equilibrates with capillary forces except in pores fully saturated with air (8, 60). By the final drainage stages (Fig. 3 *D* and *E*), air occupies most pores and throats, leaving residual water as thin films coating pore surfaces or as pendular structures in crevices.* Following primary drainage (Fig. 3*E*), imbibition commences with water injection from the bottom reservoir while maintaining constant pressure in adjacent pores. Imbibition dynamics are complicated by preexisting water films in throats, leading to diverse flow patterns (Fig. 4 *A*–*E*). They range from piston-like displacement and snap-off mechanisms to cooperative filling,† where multiple throats near air-saturated pores are simultaneously invaded by water (61, 62).

*Thin-film flow along pore surfaces is not simulated here.

†Cooperative filling is not simulated here.

Capillary Versus Viscous Fingering

The displacement of a more viscous fluid by a less viscous one in granular materials produces complex physical patterns governed by the capillary number (C_a) and viscosity ratio (M) (63). The capillary number, defined as $C_a = \mu v/\gamma$, represents the ratio of viscous to capillary forces, where μ is the dynamic viscosity, v the fluid velocity, and γ the interfacial tension. At low C_a ($C_a \ll 1$), capillary forces dominate, while high C_a ($C_a \gg 1$) signifies viscous dominated flow. The viscosity ratio M, defined as the ratio of nonwetting and wetting fluid viscosities ($M = \mu_{nw}/\mu_w$), influences flow stability and residual fluid entrapment. Together, C_a and M delineate distinct flow regimes: low C_a with $M > 1$ promotes capillary fingering, whereas high C_a and $M < 1$ drive viscous fingering and unstable invasion front under steep pressure gradients (63, 64).

Our simulations model a thin, laterally confined granular bed initially saturated with water, except for a central air-filled region (Fig. 5*A*). The bottom boundary is impermeable to constrain

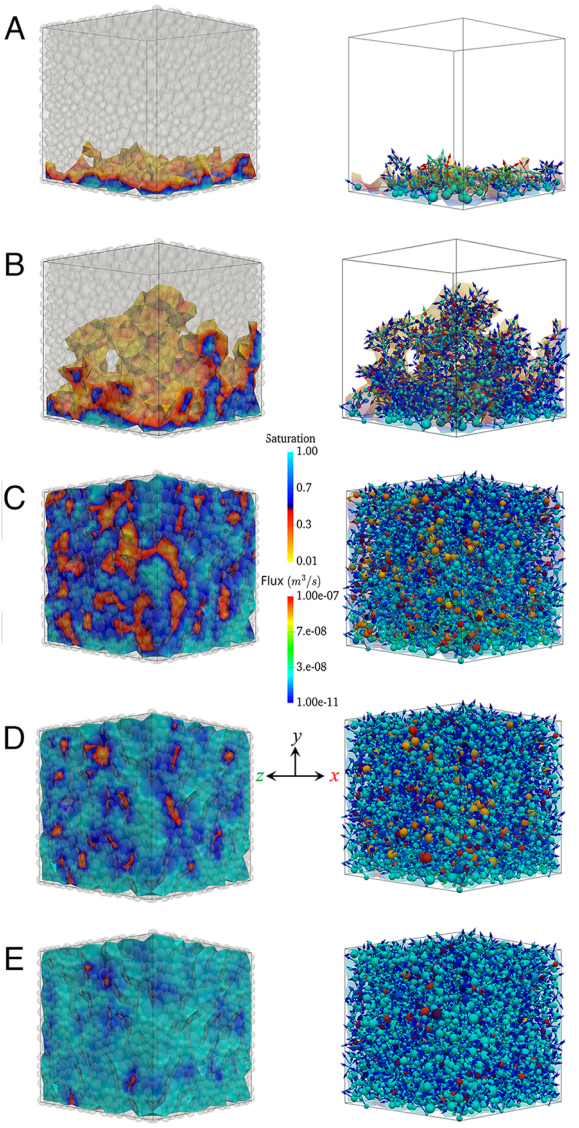

Fig. 4. Visualization of imbibition dynamics in glass beads. *Left* panels: Fluid configuration color-mapped to wetting fluid saturation. *Right* panels: Fluid flux vectors indicating invasion pathways, with color intensity scaling with flux magnitude. Pores are depicted as spheres, color-coded by local wetting fluid saturation at progressive imbibition stages: (*A*) S_r = 0.05, (*B*) S_r = 0.15, (*C*) S_r = 0.55, (*D*) S_r = 0.70, and (*E*) S_r = 0.91.

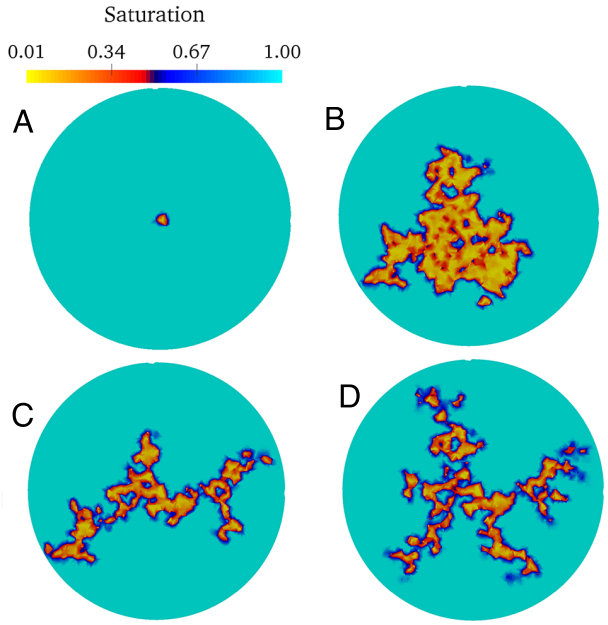

Fig. 5. A circular midsection of a thin bed of particles illustrating different fluid invasion states. (*A*) The initial state with a small air fraction at the center. (*B*) Capillary fingering occurs at a capillary number $Ca \approx 10^{-5}$. (*C*) Crossover observed at a capillary number $Ca \approx 10^{-4}$. (*D*) Viscous fingering observed at a capillary number $Ca \approx 10^{-3}$.

vertical flow, while lateral boundaries remain open. Three constant lateral water pressures (−3, −5, and −10 kPa) were imposed to drain the system, corresponding to capillary numbers $C_a \approx 10^{-5}$ (capillary-dominated), $C_a \approx 10^{-4}$ (capillary-viscous transitional in our system), and $C_a \approx 10^{-3}$ (viscosity-dominated), respectively. Fig. 5 *B*–*D* illustrate distinct air invasion patterns captured by our simulations (Movies S1 and S2) (12, 65):

- **Capillary fingering** (Fig. 5*B*): Intermittent, asymmetric air propagation governed by spatial variations in capillary entry pressure, characteristic of capillary-dominated regimes ($C_a \approx 10^{-5}$) (63).
- **Transitional fingering** (Fig. 5*C*): Hybrid morphology with partially branching and directionally growth, feathered by alternating capillary-driven burst (local pore invasions) and viscous-driven front advancement, reflecting competitive dynamics in the transitional regime ($C_a \approx 10^{-4}$).
- **Viscous fingering** (Fig. 5*D*): Continuous, radially branching air invasion with concurrent front advancement at multiple sites, driven by viscous instabilities in high-C_a regimes ($C_a \approx 10^{-3}$).

Following Raeini et al. (66), the transition of capillary-to-viscous dominance is broadly recognized near $C_a \approx 10^{-5}$. However, in our air–water system, capillary effects persist at higher C_a (10^{-4}) due to air's low viscosity and pore-scale heterogeneity, delaying viscous dominance until $C_a \approx 10^{-3}$. This aligns with prior work on gas–liquid systems, where fingering patterns (indicative of capillary dominance) emerge even at elevated C_a (61, 63).

Confined Granular Swelling in Unsaturated Flow

Swelling of confined granular materials during unsaturated flow arises from complex interactions where fluid uptake drives volumetric expansion of particles, counteracted by the confining stresses of the surrounding granular matrix. Unlike free swelling—where expansion is uniform—confinement creates spatially varying stress distributions that alter both the magnitude and kinetics of swelling. These processes are critical for applications where fluid-induced swelling risks mechanical instability or alters transport properties, such as soil mechanics under unsaturated dynamic conditions, industrial porous materials (e.g., paper, absorbents, hygienic products), and water-absorbent granular additives (49, 67–70).

Simulations. To investigate confined swelling, we modeled 3D disordered granular packing composed of polydisperse spherical particles (average radius 0.175 mm, density 2,650 kg/m^3) that represent sand-sized grains. A swellable material (density 1,200 kg/m^3, initial radius 0.25 mm) was embedded at the packing center. This material exhibits a water absorption ratio of 47 g/g, achieving a maximum swollen radius of $R_{max} = 3.6R_0$, where R_0 is the initial radius. Swelling kinetics follows a first-order rate equation controlled by a diffusion coefficient $D = 5 \times 10^{-8}$ m^2/s, governing fluid uptake and expansion under unsaturated conditions (71). The temporal evolution of particle radius R_i is described by

$$\frac{dR_i}{dt} = k_0 f_w (R_{\max} - R_i), \qquad [2]$$

where the swelling kinetic coefficient k_0 is defined by $k_0 = 3DR_i/R_0^3$, D is the diffusion coefficient, R_0 and R_i are the initial and instantaneous particle radius, respectively; $R_{\max}$ is the maximum swollen radius. The wetted fraction f_w is the ratio of the particle's water-contacting surface area to its total surface area. It ensures that swelling is dynamically coupled to local saturation state (49). In our simulations, swelling was initiated by progressively reducing water pressure while maintaining air pressure at 0 Pa.

Macroscopic responses. Fig. 6*A* illustrates grain-scale radius evolution under vertical confinement stresses σ_v. At low confinement ($\sigma_v = 0.1$ kPa), particles swell rapidly approaching their maximum equilibrium radius. In contrast, under high confinement ($\sigma_v = 1$ kPa), mechanical resistance from the granular matrix suppresses swelling (see Fig. 7 for detailed visualization of radius evolution). Fig. 6*B* tracks macroscopic porosity changes. At lower σ_v, an early stage shows decreasing porosity as swelling particles displace neighboring grains, compressing the matrix, while at a late stage, porosity increases as particle rearrangement (e.g., rolling and sliding) accommodates expansion, stabilizing once structural reconfiguration equilibrates. Under high σ_v, stiffened force chains in the granular packing limit rearrangement, causing porosity to monotonically decrease and stabilize. This highlights the competition between swelling-driven porosity reduction and confinement-governed granular adaptability via fabric changes (Movies S3 and S4) (69, 70).

Micromechanical insights. At the grain scale, swelling-induced force transmission exhibits distinct modes depending on confinement stress. Under lower confinement (Fig. 8 *A* and *B*), force chains remain sparsely distributed, with weak interparticle contact forces enabling extensive structural reconfiguration of the granular matrix. This facilitates a near-homogeneous stress distribution, allowing localized particle rearrangements to accommodate swelling with minimal resistance. Conversely, under higher confinement (Fig. 8 *C* and *D*), the force chain network evolves into a highly localized network. Percolating force chains develop, creating rigid load-bearing columns that resist volumetric expansion by redirecting swelling-induced displacements into adjacent pore spaces. This results in anisotropic deformation patterns, where expansion is constrained along

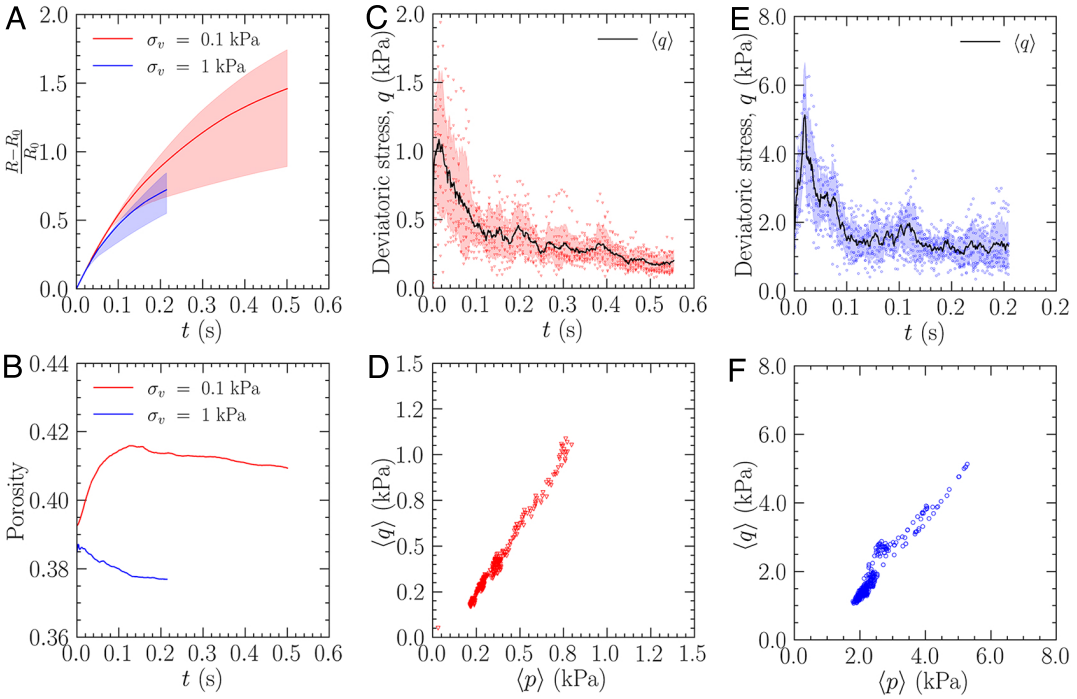

Fig. 6. (*A*) Evolution of average swellable particle radius under varying confinement $\sigma_V = 0.1$ kPa (red line) and $\sigma_V = 1$ kPa (blue line). Shaded regions indicate upper/lower bounds of particle radius variability. (*B*) Porosity evolution of the granular packing under the same confining stresses ($\sigma_V = 0.1$ and 1 kPa). Evolution of deviatoric stress and stress path under confinement: (*C*) [$\sigma_V = 0.1$ kPa]: Temporal evolution of deviatoric stress q (individual data points: markers' average $\langle q \rangle$: solid black line). The shaded region denotes one SD. (*D*) [$\sigma_V = 0.1$ kPa]: Stress–path relationship between average mean stress $\langle p \rangle$ and average deviatoric stress $\langle q \rangle$. (*E*) [$\sigma_V = 1.0$ kPa]: $q(t)$ with individual markers, average $\langle q \rangle$, and variability bounds. (*F*) $\langle p \rangle$-$\langle q \rangle$ trajectory under high confinement.

preferential pathways dictated by stress-transmitting chains-a phenomenon mirroring shear-induced fabric anisotropy in granular media (72).

In confined granular systems, particle swelling generates normal compressive forces and shear forces that drive particle sliding and force redistribution-a process mirroring stress heterogeneity observed in swelling-driven fracture networks (73). The system may evolve toward a mechanically constrained steady state, analogous to the critical state in sheared granular media but uniquely driven by internal swelling [Fig. 6 *C*–*F*: deviatoric stress accumulation (also visualized in Fig. 9) and stress path evolution highlight this transition]. Stress redistribution follows a percolation-like mechanism, where strong force chains dictate bulk mechanical behavior. Swelling-induced stresses propagate along these dominant force chains, bypassing weakly connected regions-a phenomenon reminiscent of shear band formation in densely packed systems (74). This preferential stress transmission observed in Figs. 8 and 9 underscores how local force chain

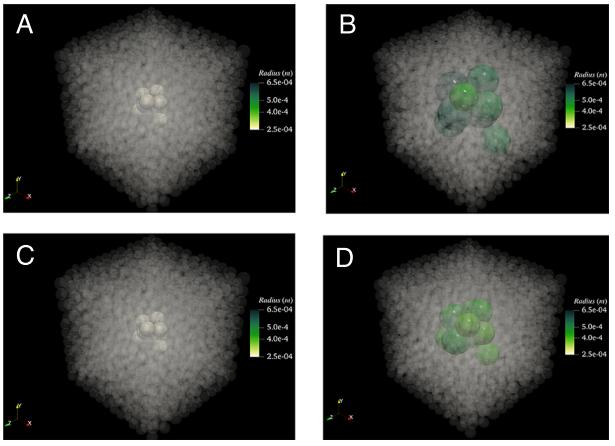

Fig. 7. (*A*) Initial particle radius distribution in a granular packing containing swellable particles under low confinement ($\sigma_V = 0.1$ kPa). (*B*) Final state under low confinement, showing expanded particles and reorganized granular fabric. (*C* and *D*) Particle expansion and the granular configuration under higher confinement ($\sigma_V = 0.1$ kPa), highlighting restricted swelling and stress-localized deformation. Color bar: particle radius (m), with green ($>3.6 \times 10^{-4}$ and yellow ($<2.5 \times 10^{-4}$) denoting swollen and unswollen states, respectively.

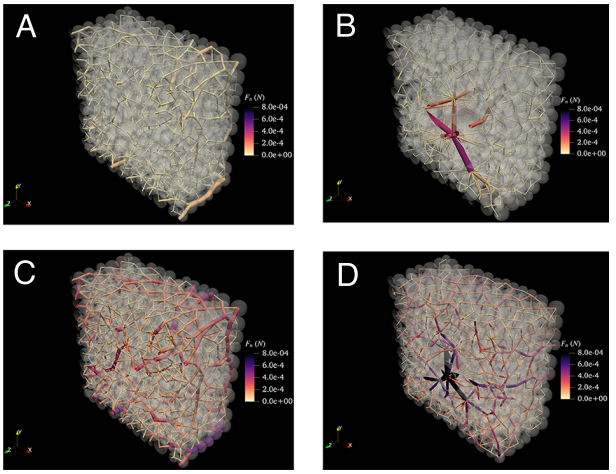

Fig. 8. Force chain evolution under different confinement. (*A* and *B*) Lower confinement ($\sigma_V = 0.1$ kPa): (*A*) Initial force chain network, and (*B*) final state after swelling-induced force redistribution. (*C* and *D*) High confinement ($\sigma_V = 1$ kPa): (*C*) Initial force chain network, and (*D*) final state showing localized force amplification. Force magnitudes are encoded by color intensity (darker hues = higher forces). Subfigures (*B*) and (*D*) emphasize how particle swelling redistributes interparticle forces, altering stress transmission pathways in the granular medium.

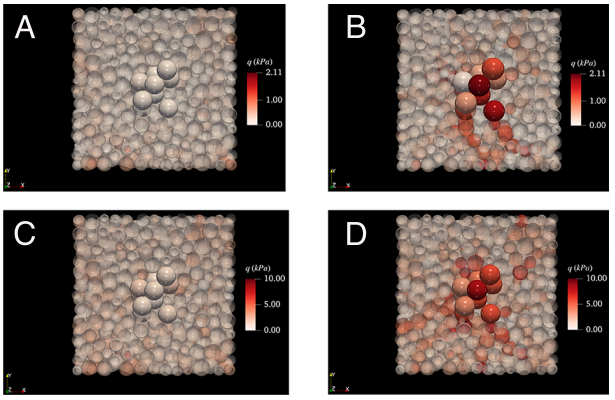

Fig. 9. Deviatoric stress distribution under (*A* and *B*) low confinement (σ_V = 0.1 kPa) and (*C* and *D*) high confinement (σ_V = 1 kPa). Subfigures (*A*) and (*C*) depict the initial stress state under the two confinements. Panel (*B*) shows the dynamic stress reconfiguration at 0.02 s for the σ_V = 0.1 kPa case, whereas (*B*) shows the localized stress amplification at t = 0.01 s for the high confinement case. Stress magnitudes are encoded by color intensity (darker = higher stress). Deviatoric stress per particle is calculated by integrating forces over each particle's Voronoi volume.

topology around swelling particles governs global granular response under confinement.

One-Dimensional Desaturation

We conducted desaturation simulations on polydisperse granular packings using PUA-DEM to unravel the hydromechanical behavior of unsaturated granular systems. Granular assemblies comprised polydisperse spheres (average radius 0.2 mm) in both dense and loose configurations, achieved by varying initial interparticle friction angles. The desaturation process was modeled under oedometer conditions, with results analyzed using dimensionless capillary pressure p^c (Eq. **3**). Key DEM and fluid parameters are detailed in *SI Appendix*, Table S3.

$$p^c = \frac{(p^{nw} - p^w)\langle r \rangle}{\gamma}, \qquad [3]$$

where $\langle r \rangle$ is the average particle radius and γ is the interfacial tension of the wetting–nonwetting fluid.

Fig. 10*A* illustrates the evolution of capillary pressure (p^c), wetting fluid saturation (S_r), and axial strain during desaturation. The ($p^c - S_r$) relationship reveals three distinct regimes: 1) Capillary regime ($p^c < 3.5$): Nonwetting fluid invasion initiates at the air entry value, preferentially occupying pores with the lowest capillary resistance (77). 2) Funicular regime ($3.5 < p^c < 4.9$): Saturation decreases abruptly due to Haines jumps-localized drainage events triggering cascading fluid displacement (Fig. 11 *D*, *Middle* panel). 3) Pendular regime ($p^c > 4.9$): Residual wetting fluid forms isolated pendular bridges in smaller capillary pores (Fig. 11 *D*, *Right* panel), stabilizing the granular matrix. Midplane fluid distributions for each regime (Fig. 11*D*) visually corroborate these dynamics, highlighting distinct invasion morphologies from connected pathways (capillary/funicular) to disconnected pendular structures.

The mechanical response of granular packings (Fig. 10*A*) transitions from initial contraction to expansion as desaturation progresses. Axial strain (ϵ_a) initially increases linearly with p^c in the capillary regime, consistent with Terzaghi's effective stress principle (σ^{yy}_{net} in Fig. 10*B*) (25). In the funicular regime, the $p^c - \epsilon_a$ relationship becomes nonlinear as declining saturation reduces effective stress. By the pendular regime, effective stress diminishes further due to the limited cohesion provided by isolated capillary bridges (Fig. 10 *C* and *D*) (11, 28, 45, 78). The probability distribution of capillary forces (Fig. 10 *C* and *D*) confirms weakening interparticle cohesion with decreasing saturation. While the loose packing follows similar trends, it exhibits notably lower average capillary forces at comparable S_r due to its reduced air-entry value and fluid retention characteristic (Fig. 10*A*). These disparities underscore how packing density modulates hydromechanical coupling by altering pore connectivity and capillary stability.

Fig. 11*A* analyzes capillary force anisotropy across different regimes. In the capillary and funicular regimes, capillary forces align directionally with fluid flow, while the pendular regime exhibits isotropic orientations (Fig. 11*D*). In high saturation regions, the capillary force anisotropy deviates from spherical symmetry, resembling capillary regime dynamics (Fig. 11 *D*, *Middle* panel, subdomain **B**), whereas low-saturation zones show isotropic capillary forces (see *SI Appendix*, Figs. S6–S8 for a detailed discussion on the explicit resolution of capillary force anisotropy using triaxial compression as test cases). Trapped wetting fluid amplifies capillary forces, inducing particle agglomeration (Fig. 11 *D*, *Right* panel, zoom). Force chain networks in Fig. 11*B* reveal particle clustering in high-saturation regions (Fig. 11*C*), with mean normal contact forces decreasing from 0.025 N from the capillary regime to 0.014 N in the pendular regime. The micromechanics-based effective stress σ'_{ij} defined in Eq. **4** incorporates fluid and interfacial tension forces, yielding a multiphase analog to Terzaghi's formulation (1, 79, 80). The results demonstrate a linear $S_r - \chi$ relationship (Fig. 10*E*) where χ denotes the Bishop's effective stress parameter, challenging the classical assumption that $\chi = S_r$. PUA-DEM predictions agree

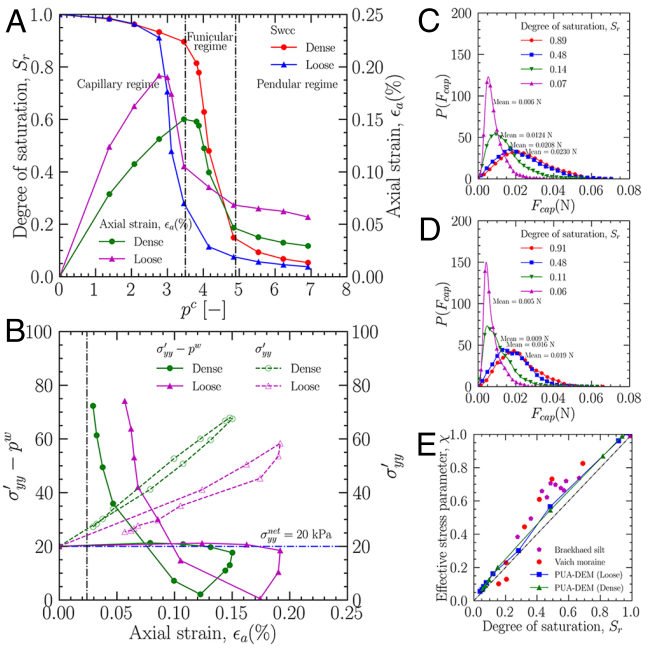

Fig. 10. Two-way hydromechanical coupling during 1D desaturation. (*A*) Hydraulic response: evolution of and $p^c - S_r$ for dense (red lines) and loose (blue lines) granular packings. (*B*) Mechanical response: Axial stress–strain response under oedometric (1D) conditions, comparing dense and loose cases. Probability distribution of the magnitude of capillary forces in (*C*) a dense granular packing and (*D*) a loose granular packing. (*E*) Comparison of Bishop's effective stress parameter χ between a dense and loose granular packing, obtained from the coupled PUA-DEM approach, and experimental results from Bishop (75) and Bishop and Blight (76).

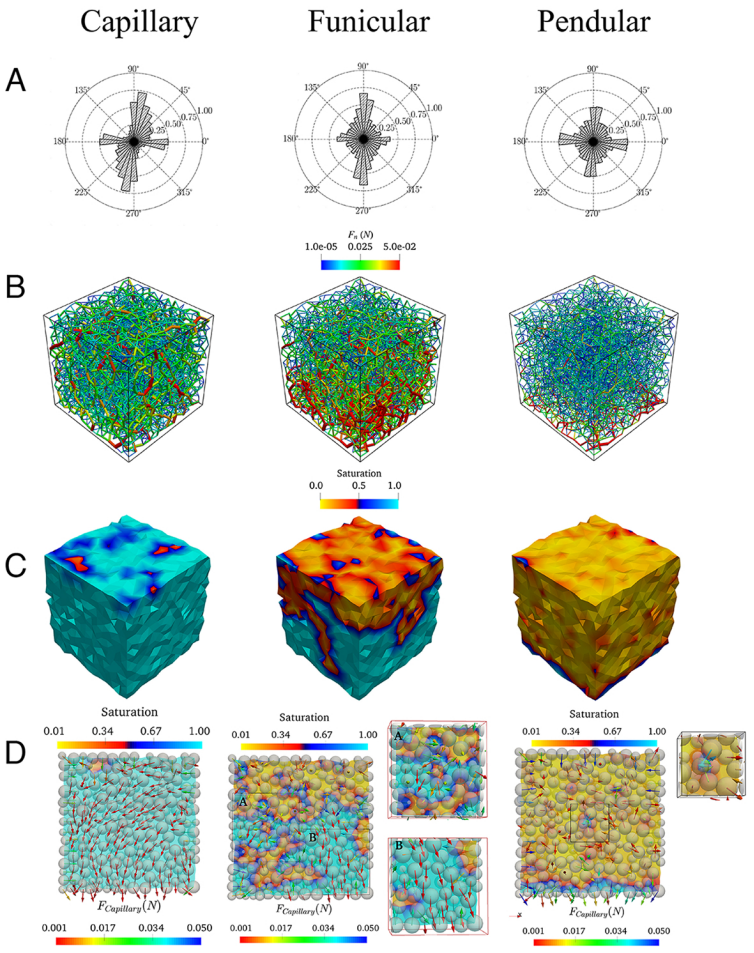

Fig. 11. Capillary force anisotropy and fluid-phase evolution across saturation regimes. (*A*) Quantified anisotropy of capillary force orientations under varying saturation conditions. (*B*) Comparative visualization of force chain network topology among capillary, funicular, and pendular states. (*C*) Spatial fluid saturation distributions across capillary, funicular, and pendular regimes, with colormap scaling from 0 (dry) to 1 (fully saturated). (*D*) Midplane (*xy*-plane) fluid morphology and capillary force dynamics (vector glyphs): *Left*: capillary regime dominated by connected fluid bridges, with vector glyphs (DEM particles) illustrating force orientation and magnitude. *Middle*: Funicular regime showing percolating fluid flusters (global saturation $S_r = 0.6$, with *Insets* highlighting subdomains **A** (fluid–solid menisci) and **B** (capillary force redistribution during cluster coalescence). *Right*: Residual pendular regime ($S_r = 0.15$) with isolated fluid ganglia exerting localized capillary forces on particles.

with experimental data in the capillary and pendular regimes but diverge in the funicular regime, likely due to the simplifications in grain shape and pore morphology.

$$\sigma_{ij} = \sigma'_{ij} + [\chi p^{w} + (1 - \chi p^{air})]\delta_{ij}. \quad [4]$$

Using the PUA-DEM framework, Bishop's effective stress σ'_{ij} is derived according to $\sigma'_{ij} = \frac{1}{V}\sum_{c=1}^{N_c} f_i^c d_j^c$, and $\chi = (\sigma'_{yy} - \sigma_{yy}^{net})/(p^n - p^w)$.

Wetting-Induced Granular Collapse

Simulations and force partitioning. A polydispersed sphere packing with a mean particle radius $\langle r \rangle = 0.3$ mm was generated within a cubic domain of dimensions $0.01 \times 0.01 \times 0.01$ m^3. Capillary bridges were introduced at particle contacts under a capillary pressure of 50 kPa, and isotropic compaction was applied using servo-controlled frictionless walls. This process yielded porosities of 0.51 and 0.47 under confining stresses of 20 and 200 kPa, respectively. Imbibition was initiated by increasing

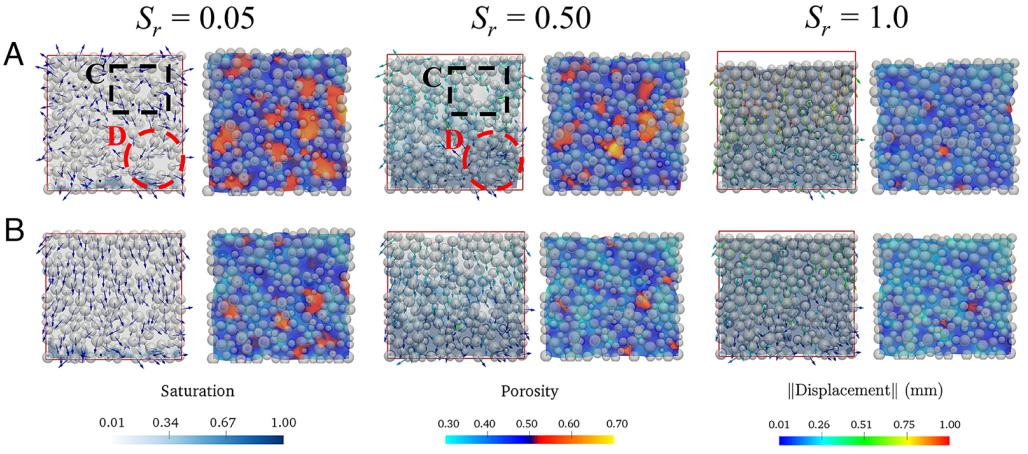

Fig. 12. Cross-sectional midplane evolution during wetting-induced collapse under vertical stresses σ_V. (*A*) $\sigma_V = 20$ kPa and (*B*) $\sigma_V = 200$ kPa: Particle displacement vectors (color-scaled by magnitude) and porosity distribution (grayscale) at low to full saturation regimes. Subdomains **C** and **D** highlight localized porosity amplification and reduction, respectively.

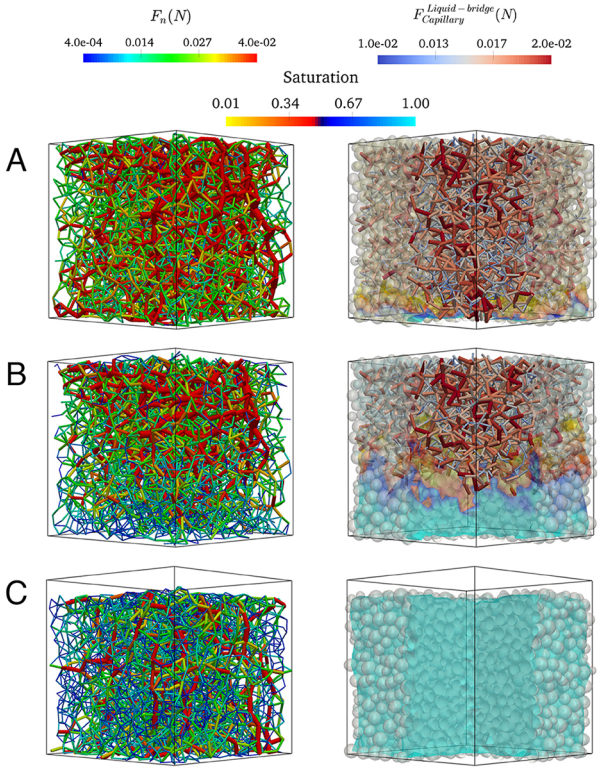

Fig. 13. Evolutions of Force chain network (*Left*) and liquid bridge network (*Right*) during wetting at water saturation under low confinement (σ_V = 20 kPa). (*A*) 0.005. (*B*) 0.50. (*C*) 1.0.

the wetting fluid pressure, following an invasion percolation process without causing snap-off. Liquid bridge coalescence with the wetting front was determined using edge information from RT decomposition, with coalescence triggered when pore saturation exceeds a predefined threshold.

The total force acting on a particle comprises contact forces (F^c) and fluid force (F^f), where F^f is partitioned into contributions from liquid bridges (F^{lb}) and funicular clusters (F^{fun}), i.e., $F^f = F^{lb} + F^{fun}$. The liquid bridge force F^{lb} is calculated using the capillary model of Scholtes et al. (80), while the funicular cluster force F^{fun} is derived from the pore-network topology (*SI Appendix*, Eq. **S23**). This partitioning ensures accurate resolution of fluid–solid interactions to capture the distinct roles of capillary bridges (localized forces) and interconnected liquid clusters (network-dependent forces) governing granular mechanics.

Microstructure evolution and pore-scale metrics. Fig. 13 and Movie S5 illustrate the evolutions of force chains and liquid bridges during wetting-induced collapse. Initially, the system exists in a metastable, partially saturated state stabilized by capillary bridges (Fig. 13*A*) (81, 82). As imbibition progresses and capillary pressure p^c decreases, fluid infiltration drives structural reorganization due to rebalancing of fluid–solid interface (Fig. 13*B*). This transition introduces a new force equilibrium stabilized by combined capillary forces from liquid bridges and funicular clusters (82). At full saturation (Fig. 13*C*), capillary bridges dissolve when the pores become fully saturated, transferring load-bearing entirely to the force chains. Fig. 12 highlights particle displacements and microscale porosity (ϕ) evolution in a clipped midsection during wetting. Under low confinements (σ_v = 20 kPa), imbibition induced significant collapse, particularly in dense, low-porosity regions (subdomain **D** marked as a circle, Fig. 12*A*), where capillary forces drove further densification. In contrast, dry regions (Subdomain **C** marked as square) expanded due to reduced capillary cohesion. High confinement (σ_v = 200 kPa) suppressed collapse due to the precompacted granular fabric, Fig. 12*B* (*SI Appendix*, Fig. S9).

Fig. 14 *A* and *B* depict probability distributions of the normalized pore radius $R_i/\langle r\rangle$, normalized pore throat radius $R_{ij}/\langle r\rangle$, and microscale pore porosity ϕ_i during wetting-induced collapse. At σ_v = 20 kPa, the initial open microstructure (characterized by a mixed Gaussian on ϕ_i: mean 0.43, SD 0.11) is gradually densified during imbibition to a state of ϕ_i with mean 0.39 and SD 0.08, with significant shifts in pore and throat radii. At σ_v = 200 kPa, minimal changes occur due to restricted particle

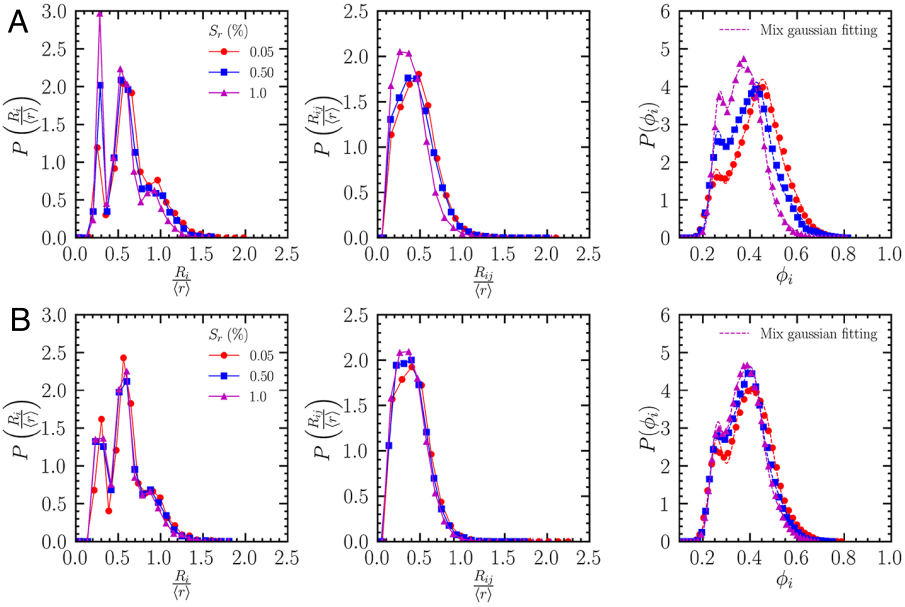

Fig. 14. Pore-scale statistical distributions under vertical stress (σ_V): Normalized pore radius ($R_i/\langle r\rangle$), normalized pore throat radius ($R_ij/\langle r\rangle$), and local porosity (ϕ_i). (*A*) σ_V = 20 kPa. (*B*) σ_V = 200 kPa. Distributions are for saturation levels S_r = 0.05, 0.50, and 1.0. Mixed Gaussian fits (dashed lines) reveal bimodal porosities.

mobility in the dense packing (Figs. 12 *B*, *Left* panel and 14 *B*, *Right* panel).

Conclusions and Outlook

We presented PUA-DEM, a coupled pore-scale micromechanical framework designed to simulate the hydromechanical behavior of partially saturated granular materials across fluid distribution regimes-from capillary, funicular to pendular. Unlike conventional pendular bridge models, PUA-DEM dynamically resolves capillary pressure at air–water interfaces in granular pores as an emergent fluid flow property rather than a predefined input. This approach enables bidirectional coupling: fluid forces are iteratively transferred to the DEM solver to update particle positions, while updated fabric packing and pore geometries inform evolving fluid pressure and saturation fields. The predictive capabilities of the framework were exemplified by five challenging hydromechanical problems: 1) drainage/imbibition cycles, 2) capillary versus viscous fingering, 3) confined granular swelling, 4) 1D desaturation, and 5) wetting-induced collapse. Key findings include:

- In confined systems, swelling-induced restructuring and mechanical constraints jointly govern equilibrium stress states and deformation pathways. High confinement suppresses particle expansion, redirecting swelling into pore spaces via percolating force chains.
- Prediction of fluid invasion patterns and strain localization for 1D desaturation process and wetting-induced collapse capture key fluid-deformation coupling and validates unsaturated soil mechanics principle.
- PUA-DEM replicated capillary-driven fluid flow and particle agglomeration. During desaturation, capillary forces transition from an anisotropic (capillary) to isotropic (pendular) regime, reflecting shifts in fluid connectivity.
- A Bishop-type effective stress equation was derived from micromechanical principles. The computed effective stress parameter (χ) correlated strongly with experimental data for sands and silts, validating the framework's ability to resolve unsaturated granular micromechanics.
- Wetting-induced collapse triggers particle aggregation and densification in imbibed regions (e.g., Subdomain D), while dry regions (Subdomain C) expand. Statistical analyses of pore radii, throat sizes, and microscale porosity (ϕ_i) quantitatively corroborate these microstructural shifts.

While the PUA-DEM framework effectively resolves key micromechanical processes, its current limitations include: 1) particle shape simplification: the assumption of idealized spherical particles neglects the irregular shapes and angularity inherent to natural granular materials, which govern interlocking, force transmission, and pore connectivity (83). Incorporating realistic particle morphologies would enhance predictions of particle rearrangement under hydromechanical loading. 2) Wettability effects: the framework does not yet account for wettability variations, which critically influence fluid invasion patterns, residual saturation, and interfacial dynamics. Integrating wettability-dependent contact angles would broaden applicability to engineered and natural systems. These limitations highlight critical opportunities for advancement, including: 1) Fluid invasion transitions: systematic studies of fluid invasion patterns across packing densities-from frictional flows in loose media to fracturing in dense states-could bridge experimental observations [e.g., Hele-Shaw cell studies (84, 85)] with granular micromechanics. Resolving pore-scale stress fields and interparticle forces during these transitions remains a key challenge. 2) High-fidelity interface modeling: enhancing resolution of dynamic 3D interfaces in irregular pore geometries would improve predictions of capillary trapping and phase displacement. Further incorporating evaporation/condensation dynamics (86) would enable simulations of hygroscopic swelling or drying-induced cracking. 3) Hybrid computational strategies: combining the Lattice Boltzmann Method (LBM) with adaptive mesh refinement (36)-fine grids near interfaces, coarse grids in single-phase regions-could optimize accuracy and efficiency. Hybrid pore network model with LBM (PNM-LBM) approaches could resolve complex fluid interfaces while maintaining pore-scale relationships for permeability and capillary pressure. These advancements would expand PUA-DEM's capacity in simulating wetting/drying cycles, reactive transport, and multiphase flows in heterogeneous granular systems, building on its current successes.

Materials and Methods

We developed PUA-DEM, a pore-scale micromechanical framework coupling the DEM with a pore-network fluid solver to simulate unsaturated hydromechanics in granular media (*SI Appendix*). Our framework integrates four components. 1) **Pore network construction**: Regular triangulation discretizes void space into tetrahedral pores/throats, with merging algorithm simplifying polydisperse packings while preserving connectivity (Figs. 1 *A*–*C*). 2) **Fluid flow modeling**: Single-phase flow follows Darcy's law (*SI Appendix*, Eqs. **S1**–**S6**); two-phase flow uses an IMPES scheme with capillary pressure–saturation relationships and invasion criteria (*SI Appendix*, Eqs. **S15**, **S18**, and **S19**). 3) **Hydromechanical coupling**: Fluid forces (pressure and interfacial tension) at pore throats are projected onto particles via geometric weights (*SI Appendix*, Eqs. **S23**–**S29**) (40, 45). DEM resolves contact mechanics, while fluid states update iteratively with pore geometry (*SI Appendix*, Fig. S2). 4) **Validation**: Benchmarked against 1D Darcy flow (analytical) and experimental (glass beads/Ottawa sand; *SI Appendix*, Figs. S4 and S5 and Fig. 2 *A* and *B*). Key assumptions: spherical particles (to approximate natural grains), homogeneous wettability (no hysteresis), and neglected thin-film flow and osmotic effects.

Data, Materials, and Software Availability. All study data are included in the article and/or supporting information.

ACKNOWLEDGMENTS. The study was financially supported by Research Grants Council of Hong Kong through Nos. GRF 16203123, CRF C7082-22G, TRS T22-607/24N, and T22-606/23-R, and NSF of China under Project 52439001.

Author affiliations: [a]Department of Civil and Environmental Engineering, Hong Kong University of Science and Technology, Clearwater Bay, Kowloon 999077, Hong Kong, Special Administrative Region of China; and [b]Faculty of Geosciences, Utrecht University, Utrecht 3584 CB, The Netherlands

Author contributions: A.P.D. and J.Z. designed research; A.P.D. performed research; A.P.D. and J.Z. analyzed data; and A.P.D., J.Z., and T.S. wrote the paper.

1. Kv. Terzaghi, "The shearing resistance of saturated soils and the angle between the planes of shear" in *First International Conference on Soil Mechanics* (1936), vol. 1, pp. 54–59.
2. M. T. Van Genuchten, A closed-form equation for predicting the hydraulic conductivity of unsaturated soils. *Soil Sci. Soc. Am. J.* **44**, 892–898 (1980).
3. L. Cueto-Felgueroso, R. Juanes, Nonlocal interface dynamics and pattern formation in gravity-driven unsaturated flow through porous media. *Phys. Rev. Lett.* **101**, 244504 (2008).
4. M. L. Szulczewski, C. W. MacMinn, H. J. Herzog, R. Juanes, Lifetime of carbon capture and storage as a climate-change mitigation technology. *Proc. Natl. Acad. Sci. U.S.A.* **109**, 5185–5189 (2012).
5. S. Bachu, Review of CO_2 storage efficiency in deep saline aquifers. *Int. J. Greenhouse Gas Control* **40**, 188–202 (2015).
6. P. M. Adler, H. Brenner, Multiphase flow in porous media. *Annu. Rev. Fluid Mech.* **20**, 35–59 (1988).
7. J. Bear, *Dynamics of Fluids in Porous Media* (Courier Corporation, 2013).
8. M. J. Blunt, M. D. Jackson, M. Piri, P. H. Valvatne, Detailed physics, predictive capabilities and macroscopic consequences for pore-network models of multiphase flow. *Adv. Water Resour.* **25**, 1069–1089 (2002).

9. Q. Kang, D. Zhang, S. Chen, Simulation of dissolution and precipitation in porous media. *J. Geophys. Res. [Solid Earth]* **108**, 2505 (2003).
10. C. Soulaine, S. Roman, A. Kovscek, H. A. Tchelepi, Mineral dissolution and wormholing from a pore-scale perspective. *J. Fluid Mech. Res.* **827**, 457–483 (2017).
11. T. Zhou, K. Ioannidou, F. J. Ulm, M. Z. Bazant, R. M. Pellenq, Multiscale poromechanics of wet cement paste. *Proc. Natl. Acad. Sci. U.S.A.* **116**, 10652–10657 (2019).
12. R. Holtzman, M. L. Szulczewski, R. Juanes, Capillary fracturing in granular media. *Phys. Rev. Lett.* **108**, 264504 (2012).
13. Y. Meng, W. Li, R. Juanes, Fracturing in wet granular media illuminated by photoporomechanics. *Phys. Rev. Appl.* **18**, 064081 (2022).
14. A. Guével, Y. Meng, C. Peco, R. Juanes, J. E. Dolbow, A Darcy–Cahn–Hilliard model of multiphase fluid-driven fracture. *J. Mech. Phys. Solids* **181**, 105427 (2023).
15. O. W. Paulin, L. C. Morrow, M. G. Hennessy, C. W. MacMinn, Fluid–fluid phase separation in a soft porous medium. *J. Mech. Phys. Solids* **164**, 104892 (2022).
16. F. J. Carrillo, I. C. Bourg, A Darcy–Brinkman–Biot approach to modeling the hydrology and mechanics of porous media containing macropores and deformable microporous regions. *Water Resour. Res.* **55**, 8096–8121 (2019).
17. F. J. Carrillo, I. C. Bourg, Modeling multiphase flow within and around deformable porous materials: A Darcy–Brinkman–Biot approach. *Water Resour. Res.* **57**, e2020WR028734 (2021).
18. E. E. Alonso, A. Gens, A. Josa, A constitutive model for partially saturated soils. *Geotechnique* **40**, 405–430 (1990).
19. B. François, L. Laloui, ACMEG-TS: A constitutive model for unsaturated soils under non-isothermal conditions. *Int. J. Numer. Anal. Meth. Geomech.* **32**, 1955–1988 (2008).
20. D. Sheng, D. G. Fredlund, A. Gens, A new modelling approach for unsaturated soils using independent stress variables. *Can. Geotech. J.* **45**, 511–534 (2008).
21. R. I. Borja, A. Koliji, On the effective stress in unsaturated porous continua with double porosity. *J. Mech. Phys. Solids* **57**, 1182–1193 (2009).
22. M. Nuth, L. Laloui, Advances in modelling hysteretic water retention curve in deformable soils. *Comput. Geotech.* **35**, 835–844 (2008).
23. P. A. Cundall, O. D. Strack, A discrete numerical model for granular assemblies. *Geotechnique* **29**, 47–65 (1979).
24. M. Scheel *et al*., Morphological clues to wet granular pile stability. *Nat. Mater.* **7**, 189–193 (2008).
25. J. Duriez, M. Eghbalian, R. Wan, F. Darve, The micromechanical nature of stresses in triphasic granular media with interfaces. *J. Mech. Phys. Solids* **99**, 495–511 (2017).
26. M. Jiang, T. Li, H. Hu, C. Thornton, DEM analyses of one-dimensional compression and collapse behaviour of unsaturated structural loess. *Comput. Geotech.* **60**, 47–60 (2014).
27. K. Melnikov, R. Mani, F. K. Wittel, M. Thielmann, H. J. Herrmann, Grain-scale modeling of arbitrary fluid saturation in random packings. *Phys. Rev. E* **92**, 022206 (2015).
28. X. Liu, A. Zhou, S. L. Shen, J. Li, D. Sheng, A micro-mechanical model for unsaturated soils based on dem. *Comput. Methods Appl. Mech. Eng.* **368**, 113183 (2020).
29. F. Jiang, H. Liu, X. Chen, T. Tsuji, A coupled LBM-DEM method for simulating the multiphase fluid–solid interaction problem. *J. Comput. Phys.* **454**, 110963 (2022).
30. T. Morimoto, B. Zhao, D. M. Taborda, C. O'Sullivan, Critical appraisal of pore network models to simulate fluid flow through assemblies of spherical particles. *Comput. Geotech.* **150**, 104900 (2022).
31. Z. Shen, G. Wang, D. Huang, F. Jin, A resolved CFD-DEM coupling model for modeling two-phase fluids interaction with irregularly shaped particles. *J. Comput. Phys.* **448**, 110695 (2022).
32. Z. Lai, J. Zhao, S. Zhao, L. Huang, Signed distance field enhanced fully resolved CFD-DEM for simulation of granular flows involving multiphase fluids and irregularly shaped particles. *Comput. Methods Appl. Mech. Eng.* **414**, 116195 (2023).
33. H. Liu *et al*., Multiphase lattice Boltzmann simulations for porous media applications: A review. *Comput. Geosci.* **20**, 777–805 (2016).
34. H. Warda, S. Haddara, E. Wahba, M. Sedahmed, Lattice Boltzmann simulations of the capillary pressure bump phenomenon in heterogeneous porous media. *J. Pet. Sci. Eng.* **157**, 558–569 (2017).
35. N. Younes *et al*., DEM-LBM coupling for partially saturated granular assemblies. *Comput. Geotech.* **162**, 105677 (2023).
36. E. P. Montellá, C. Yuan, B. Chareyre, A. Gens, Hybrid multi-scale model for partially saturated media based on a pore network approach and lattice Boltzmann method. *Adv. Water Resour.* **144**, 103709 (2020).
37. A. Q. Raeini, M. J. Blunt, B. Bijeljic, Modelling two-phase flow in porous media at the pore scale using the volume-of-fluid method. *J. Comput. Phys.* **231**, 5653–5668 (2012).
38. M. Shams, A. Q. Raeini, M. J. Blunt, B. Bijeljic, A numerical model of two-phase flow at the micro-scale using the volume-of-fluid method. *J. Comput. Phys.* **357**, 159–182 (2018).
39. A. Jain, R. Juanes, Preferential mode of gas invasion in sediments: Grain-scale mechanistic model of coupled multiphase fluid flow and sediment mechanics. *J. Geophys. Res. [Solid Earth]* **114**, B08101 (2009).
40. E. Catalano, B. Chareyre, E. Barthélemy, Pore-scale modeling of fluid–particles interaction and emerging poromechanical effects. *Int. J. Numer. Anal. Meth. Geomech.* **38**, 51–71 (2014).
41. A. Sufian, C. Knight, C. O'Sullivan, B. van Wachem, D. Dini, Ability of a pore network model to predict fluid flow and drag in saturated granular materials. *Comput. Geotech.* **110**, 344–366 (2019).
42. J. Zhao, F. Qin, D. Derome, Q. Kang, J. Carmeliet, Improved pore network models to simulate single-phase flow in porous media by coupling with lattice Boltzmann method. *Adv. Water Resour.* **145**, 103738 (2020).
43. R. A. Caulk, Micro-macro modeling of the long-term behavior of well-seals under hydraulic-gas loading using the Discrete Element Method (DEM), PhD thesis, Université Grenoble Alpes, Grenoble, France (2022).
44. K. Melnikov, F. K. Wittel, H. J. Herrmann, Micro-mechanical failure analysis of wet granular matter. *Acta Geotech.* **11**, 539–548 (2016).
45. C. Yuan, B. Chareyre, A pore-scale method for hydromechanical coupling in deformable granular media. *Comput. Methods Appl. Mech. Eng.* **318**, 1066–1079 (2017).
46. T. Sweijen, B. Chareyre, S. M. Hassanizadeh, N. Karadimitriou, Grain-scale modelling of swelling granular materials: Application to super absorbent polymers. *Powder Technol.* **318**, 411–422 (2017).
47. B. Chareyre, A. Cortis, E. Catalano, E. Barthélemy, Pore-scale modeling of viscous flow and induced forces in dense sphere packings. *Transp. Porous Media* **94**, 595–615 (2012).
48. T. Sweijen, S. M. Hassanizadeh, B. Chareyre, L. Zhuang, Dynamic pore-scale model of drainage in granular porous media: The pore-unit assembly method. *Water Resour. Res.* **54**, 4193–4213 (2018).
49. T. Sweijen, S. M. Hassanizadeh, B. Chareyre, Unsaturated flow in a packing of swelling particles: A grain-scale model. *Adv. Water Resour.* **142**, 103642 (2020).
50. K. A. Culligan *et al*., Interfacial area measurements for unsaturated flow through a porous medium. *Water Resour. Res.* **40**, W12413 (2004).
51. B. Chareyre, L. Briançon, P. Villard, Theoretical versus experimental modeling of the anchorage capacity of geotextiles in trenches. *Geosynth. Int.* **9**, 97–123 (2002).
52. A. Vidales, J. Riccardo, G. Zgrablich, Pore-level modelling of wetting on correlated porous media. *J. Phys. D: Appl. Phys.* **31**, 2861 (1998).
53. K. Singh, T. Bultreys, A. Q. Raeini, M. Shams, M. J. Blunt, New type of pore-snap-off and displacement correlations in imbibition. *J. Colloid Interface Sci.* **609**, 384–392 (2022).
54. M. Mohsin Thakur, D. Penumadu, C. Bauer, Capillary suction measurements in granular materials and direct numerical simulations using X-ray computed tomography microstructure. *J. Geotech. Geoenviron. Eng.* **146**, 04019121 (2020).
55. J. E. McClure *et al*., Geometric state function for two-fluid flow in porous media. *Phys. Rev. Fluids* **3**, 084306 (2018).
56. K. J. Måløy, L. Furuberg, J. Feder, T. Jøssang, Dynamics of slow drainage in porous media. *Phys. Rev. Lett.* **68**, 2161 (1992).
57. Z. Sun, J. C. Santamarina, Haines jumps: Pore scale mechanisms. *Phys. Rev. E* **100**, 023115 (2019).
58. L. Xu, S. Davies, A. B. Schofield, D. A. Weitz, Dynamics of drying in 3D porous media. *Phys. Rev. Lett.* **101**, 094502 (2008).
59. R. Holtzman, R. Juanes, Crossover from fingering to fracturing in deformable disordered media. *Phys. Rev. E* **82**, 046305 (2010).
60. D. Wilkinson, J. F. Willemsen, Invasion percolation: A new form of percolation theory. *J. Phys. A: Math. Gen.* **16**, 3365 (1983).
61. R. Holtzman, E. Segre, Wettability stabilizes fluid invasion into porous media via nonlocal, cooperative pore filling. *Phys. Rev. Lett.* **115**, 164501 (2015).
62. R. Holtzman, Effects of pore-scale disorder on fluid displacement in partially-wettable porous media. *Sci. Rep.* **6**, 36221 (2016).
63. R. Lenormand, E. Touboul, C. Zarcone, Numerical models and experiments on immiscible displacements in porous media. *J. Fluid Mech. Res.* **189**, 165–187 (1988).
64. V. Joekar-Niasar, S. Hassanizadeh, Analysis of fundamentals of two-phase flow in porous media using dynamic pore-network models: A review. *Crit. Rev. Environ. Sci. Technol.* **42**, 1895–1976 (2012).
65. G. M. Homsy, Viscous fingering in porous media. *Annu. Rev. Fluid Mech.* **19**, 271–311 (1987).
66. A. Q. Raeini, M. J. Blunt, B. Bijeljic, Direct simulations of two-phase flow on micro-CT images of porous media and upscaling of pore-scale forces. *Adv. Water Resour.* **74**, 116–126 (2014).
67. V. Kapur, J. C. Charkoudian, S. B. Kessler, J. L. Anderson, Hydrodynamic permeability of hydrogels stabilized within porous membranes. *Ind. Eng. Chem. Res.* **35**, 3179–3185 (1996).
68. T. Bertrand, J. Peixinho, S. Mukhopadhyay, C. W. MacMinn, Dynamics of swelling and drying in a spherical gel. *Phys. Rev. Appl.* **6**, 064010 (2016).
69. J. F. Louf, N. B. Lu, M. G. O'Connell, H. J. Cho, S. S. Datta, Under pressure: Hydrogel swelling in a granular medium. *Sci. Adv.* **7**, eabd2711 (2021).
70. I. Vego, A. Tengattini, E. Andò, N. Lenoir, G. Viggiani, The effect of high relative humidity on a network of water-sensitive particles (couscous) as revealed by in situ X-ray tomography. *Soft Matter* **18**, 4747–4755 (2022).
71. T. Sweijen, E. Nikooee, S. M. Hassanizadeh, B. Chareyre, The effects of swelling and porosity change on capillarity: DEM coupled with a pore-unit assembly method. *Transp. Porous Media* **113**, 207–226 (2016).
72. N. Guo, J. Zhao, The signature of shear-induced anisotropy in granular media. *Comput. Geotech.* **47**, 1–15 (2013).
73. M. S. El Youssoufi, J. Y. Delenne, F. Radjai, Self-stresses and crack formation by particle swelling in cohesive granular media. *Phys. Rev. E* **71**, 051307 (2005).
74. R. Kawamoto, E. Andò, G. Viggiani, J. E. Andrade, All you need is shape: Predicting shear banding in sand with LS-DEM. *J. Mech. Phys. Solids* **111**, 375–392 (2018).
75. A. W. Bishop, "The experimental study of partly saturated soil in the triaxial apparatus" in *Proceedings of the Fifth International Conference on Soil Mechanics and Foundation Engineering* (Paris, 1961), vol. 1, pp. 13–21.
76. A. W. Bishop, G. Blight, Some aspects of effective stress in saturated and partly saturated soils. *Geotechnique* **13**, 177–197 (1963).
77. D. Fredlund, H. Rahardjo, M. Fredlund, *Unsaturated Soil Mechanics in Engineering Practice* (John Wiley & Sons, Inc., Hoboken, NJ, 2012).
78. H. Schubert, Capillary forces-modeling and application in particulate technology. *Powder Technol.* **37**, 105–116 (1984).
79. J. Christoffersen, M. M. Mehrabadi, S. Nemat-Nasser, A micromechanical description of granular material behavior. *J. Appl. Mech.* **48**, 339–344 (1981).
80. L. Scholtès, B. Chareyre, F. Nicot, F. Darve, Micromechanics of granular materials with capillary effects. *Int. J. Eng. Sci.* **47**, 64–75 (2009).
81. L. Barden, A. McGown, K. Collins, The collapse mechanism in partly saturated soil. *Eng. Geol.* **7**, 49–60 (1973).
82. C. Yuan, M. Moscariello, S. Cuomo, B. Chareyre, Numerical simulation of wetting-induced collapse in partially saturated granular soils. *Granular Matter* **21**, 1–16 (2019).
83. J. Zhao, S. Zhao, S. Luding, The role of particle shape in computational modelling of granular matter. *Nat. Rev. Phys.* **5**, 505–525 (2023).
84. B. Sandnes, E. Flekkøy, H. Knudsen, K. Måløy, H. See, Patterns and flow in frictional fluid dynamics. *Nat. Commun.* **2**, 288 (2011).
85. R. Juanes, Y. Meng, B. K. Primkulov, Multiphase flow and granular mechanics. *Phys. Rev. Fluids* **5**, 110516 (2020).
86. O. Borgman, R. Holtzman, Impact of matrix deformations on drying of granular materials. *Int. J. Heat Mass Transfer* **153**, 119634 (2020).